

Observations of Enhanced Diapycnal Mixing near the Hawaiian Ridge

T. D. FINNIGAN, D. S. LUTHER, AND R. LUKAS

Department of Oceanography, University of Hawaii, Honolulu, Hawaii

(Manuscript received 4 June 2001, in final form 22 January 2002)

ABSTRACT

Profiles of potential density obtained from CTD casts at two stations at different distances from the Hawaiian ridge are examined for evidence of diapycnal turbulent mixing as indicated by density inversions and internal-wave vertical strain. Results from independent casts are used to produce ensemble-averaged vertical distributions for the number of inversions and the Thorpe scale. Both parameters were found to be higher over the slope of the topography at 2500-m depth than in the deep ocean, 110 km to the north. Thorpe scale-based estimates of the rate of dissipation of turbulent kinetic energy and turbulent vertical diffusivity are elevated by an order of magnitude over the slope relative to deep ocean background levels. The vertical distributions of these mixing parameters are nonuniform and exhibit signs of locally enhanced dissipation, possibly due to internal tides generated at the ridge. At the deep station, turbulence is at background levels from the surface down to 2000 m. Below this, a localized zone of enhanced mixing is observed, within which the dissipation rate is $O(10^{-9} \text{ W kg}^{-1})$ and turbulent diffusivity is greater than $O(10^{-4} \text{ m}^2 \text{ s}^{-1})$, perhaps due to an internal tide ray originating at the ridge. The full-depth topographical enhancement of mixing near the ridge also appears in the vertical strain field. Estimates of dissipation rate and turbulent diffusivity, based on an internal wave-wave interaction model, give results similar to direct Thorpe scale methods, except in weakly stratified environments where both methods are subject to uncertainty. Near the topography, the variation in mixing intensity observed between casts is sensitive to sporadic large mixing events, which are triggered by internal waves associated with the spring tide. The upper portion of the water column (stronger stratification) is more responsive to the tide than the deep regions.

1. Introduction

Stratification in the ocean interior is generally characterized by a gradual increase of density with depth. Aside from compression by hydrostatic pressure, the traditional 1D advection-diffusion models suggest that the vertical structure beneath the thermocline and above the bottom waters is maintained by a diffusive flux of heat and mass. Microstructure measurements in the ocean interior (e.g., Gregg 1987; Toole et al. 1994) have produced turbulent mass flux values that are too small to balance the vertical upwelling component in bulk one-dimensional advection-diffusion models (e.g., Munk 1966; Munk and Wunsch 1998). One explanation is that most of the deep ocean mixing is initiated at, and occurs near to, abrupt topographical features such as island chains and ridges (e.g., Munk and Wunsch 1998), with the rest of the ocean being occupied by low background levels of turbulence and nearly laminar flow. At isolated topographic features, energy is transferred from relatively large-scale barotropic and baroclinic motions to much smaller-scale baroclinic motions.

The responsible processes can lead to mixing near topography with subsequent lateral spreading of mixed fluid (e.g., Armi 1978) and to radiation of energy away from topography with possible enhancement of the mixing farther away (e.g., Polzin et al. 1997). An understanding of these energy transfer and mixing processes is crucial to advancement of our knowledge of the heat and energy budgets of the ocean, and therefore, to modeling of the global climate system.

The islands of Hawaii represent the highest peaks of a long bathymetric ridge where barotropic tidal energy is converted to baroclinic energy. The resulting low-mode internal tides have been observed, in altimeter data, to emanate from the shallow subsurface regions that link the islands (Ray and Mitchum 1996, 1997). Numerical modeling by Merrifield et al. (2001) has also demonstrated the effectiveness of the Hawaiian ridge at scattering M_2 tidal energy into low-mode internal waves.

There are several possible energy pathways between low-mode internal waves and turbulence. For specific slopes of the seafloor, critical reflection of internal waves can lead to instabilities and subsequent mixing both very near the boundary and hundreds of meters into the water column above (e.g., Phillips 1977; Ericksen 1985; Garrett 1991). Steady and time-dependent currents (including barotropic and low-mode baroclinic

Corresponding author address: Dr. D. S. Luther, SOEST, Dept. of Oceanography, 1000 Pope Road, Marine Sciences Bldg. 205, Honolulu, HI 96822.
E-mail: dluther@soest.hawaii.edu

tidal currents) passing over a rough bottom boundary can generate small-scale internal waves that propagate vertically, interfere with each other, become unstable, and produce turbulent mixing (e.g., Bell 1975). These mechanisms have been used to explain observations of enhanced turbulence near steep slopes (Toole et al. 1997) and over rough topography (Polzin et al. 1997; Ledwell et al. 2000). While some of the locally generated baroclinic energy may be dissipated in the near field, a detectable portion of it is also radiated away from the topography (e.g., the internal tide propagation observed by Ray and Mitchum 1996, 1997). The “escaping” waves can elevate shear and strain farther away and thus enhance mixing in the deep ocean. However, it is not clear how far away from the energy source enhanced mixing can be maintained by, for instance, the dispersive internal tide.

We describe possible signatures of mixing near the Hawaiian ridge as recorded in conductivity–temperature–depth profiles taken during 1994–95 as part of the Hawaii Ocean Time Series (HOT) program (Karl and Lukas 1996). Data are analyzed from two locations, 25 and 135 km from the crest of the Hawaiian ridge. Results are used to demonstrate the topographic enhancement of mixing near the ridge and to provide some evidence for a tidal modulation of mixing intensity even at 135 km from the ridge. Results also provide incentive to the community of oceanographers that is interested in estimating small-scale mixing parameters from finescale observations using standard CTD instrumentation.

The measurements and data processing are described in the following section. In section 2 we describe a method for detecting turbulent overturns. The results are then used to estimate the rate of dissipation of turbulent kinetic energy (section 3). We also present vertical strain spectra and again estimate dissipation using a parameterization based on internal wave–wave interaction theory. The dissipation results are discussed in relation to their proximity to the Hawaiian ridge. Results are then analyzed with respect to an observed temporal signal of the dynamic height (section 4). A connection between the baroclinic tide and near-field mixing is thus investigated. Conclusions appear in section 5.

2. CTD measurements

a. Measurement locations

Since October 1988, the HOT program has included monthly cruises to a number of sites in the vicinity of the island of Oahu, Hawaii. The program serves multidisciplinary oceanography studies and has the overall aim of quantifying long-term variability in the biology, chemistry, and hydrography at a representative site in the subtropical Pacific (Karl and Lukas 1996). The HOT deep-water station, ALOHA (station 2: 22°45′N, 158°0′W), is approximately 100 km north of Oahu in an area of relatively flat bathymetry and 4800-m depth

(Fig. 1). Cruises are made to this site approximately once each month and measurements are acquired for 3 days. Two CTD casts per cruise (on average) are made over the full depth of the water column.

Among the other stations visited less frequently is one located off the northwest tip (Kaena Point) of Oahu. This station (station 6: 21°50.8′N, 158°21.8′W) is situated over the north slope of the Hawaiian ridge where the depth is about 2500 m (Fig. 1). Numerical modeling by Merrifield et al. (2001) indicates this ridge is a region of strong internal tide generation. The baroclinic waves that emanate from the generation zones exhibit both low-mode and ray-like structures, possibly leading to enhanced shear and mixing near Kaena Point (station 6).

Figure 2 shows the ridge topography along the section line shown in Fig. 1. Average density profiles, derived from CTD results are shown at each station location along with bin-averaged values of buoyancy frequency, $N = [g\rho_0^{-1}(d\rho/dz)]^{1/2}$, where ρ_0 is a reference density. For N , the vertical density gradient $d\rho/dz$ was computed using a 10-m finite difference and results were averaged within each bin and over all CTD casts. The depth bins, each spanning 300 m in the vertical, will be used throughout this paper for presentation of statistical results. In general, this region north of the Hawaiian ridge is characterized by a surface mixed layer down to about 50 m, a sharp pycnocline to about 400 m, and a gradual increase in density with depth below this.

b. Data acquisition and processing

Data for the present study were acquired on 15 HOT cruises that visited both station 2 and station 6 during 1994–95. While stationary at each site, the ship deployed a CTD package which recorded one full-depth profile at station 6 and up to two full-depth profiles at station 2. The results presented here are derived from 15 CTD profiles acquired at station 6 and 25 CTD profiles acquired at station 2. At station 2, additional deployments to the 1000-db level were also made but these are not considered here.

Data were collected using a Seabird 9-11 Plus CTD with dual sensors sampling at the maximum rate of 24 Hz. Sensors were located on the bottom end of the rosette package. Only data collected during downcasts are used here to avoid contamination by the wake of the CTD/rosette package. The data were screened for missing points and spikes with a nine-point running median filter. Temperature and conductivity values were aligned in time to correct for lag effects. The data were averaged to half-second (2 Hz) values and then pressure, temperature, and conductivity calibrations and corrections were applied (for details, see Lukas and Santiago-Mandujano 1996 and the HOT data reports; cf. Santiago-Mandujano et al. 1999). Velocity and acceleration limits were applied to eliminate data points that may have been contaminated by wake effects due to ship roll. The 2-

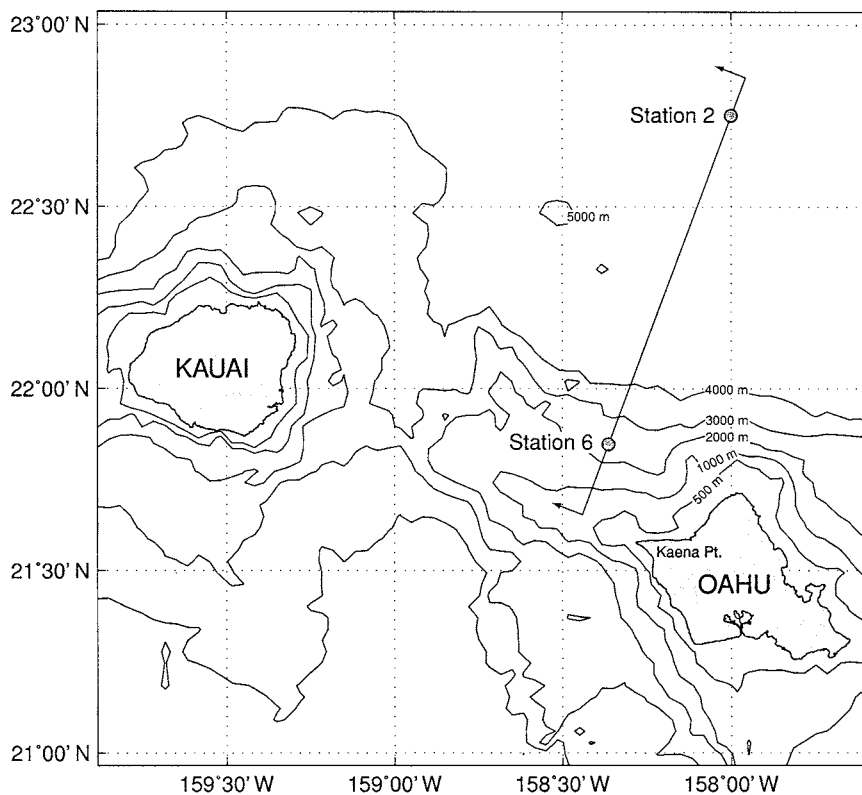


FIG. 1. Depth contours and measurement locations.

Hz data were discarded during periods where ship motion caused the CTD to exceed velocity and acceleration limits.

For the sections of data analyzed, the CTD package traveled vertically at speeds of $0.6\text{--}1.0\text{ m s}^{-1}$ and the vertical sample density for 2-Hz data is therefore $0.3\text{ m} \leq \delta z \leq 0.5\text{ m}$. As we demonstrate in the following section, this resolution is adequate for detecting and resolving turbulent overturns with a minimum vertical length scale of about 2.0 m.

c. Turbulent overturns

The first method we consider for identifying and quantifying mixing involves finding turbulent inversions or overturns in the CTD profiles. In later sections we also investigate mixing using a parameterization of the vertical strain.

A turbulent overturn is a patch of actively mixing fluid. In simple terms, one can imagine a limited region within which the destabilizing tendency of velocity shear is strong enough to overcome the stabilizing effect of vertical stratification. In such instances, the Richardson number falls below the critical value of 0.25 and isopycnals roll up and overturn, leaving behind a density inversion, or gravitationally unstable region. Diapycnal density gradients are intensified at small scales by the roll up, and diffusion is therefore enhanced by the pro-

cess (Winters and D'Asaro 1996). Unstable collapse of the overturn structure may also occur, leading more quickly to a dormant patch of uniform density fluid (Thorpe 1973).

In the present context, we assume that the shear which drives the mixing is largely due to internal waves. In the vicinity of the Hawaiian ridge the internal wave field includes topographically generated baroclinic tidal components, which are expected to enhance shear and strain above open ocean levels. We are interested in identifying turbulent overturns that result from these processes.

1) RESOLUTION

Measurement resolution imposes certain constraints on the accurate detection of overturns. As suggested by Galbraith and Kelley (1996), about five sample points are required to adequately define an overturn. The spatial resolution of the 2-Hz data sets a minimum size limit for overturns. In an effort to detect as many overturns as possible, yet avoid retaining underresolved or spurious overturns, we use the mean sample resolution $\delta z = 0.4\text{ m}$ and adhere to the constraint that no overturns with vertical dimensions smaller than

$$L_{z,\min} \approx 5\delta z = 2.0\text{ m} \quad (1)$$

are resolvable in our data. Instrument noise associated

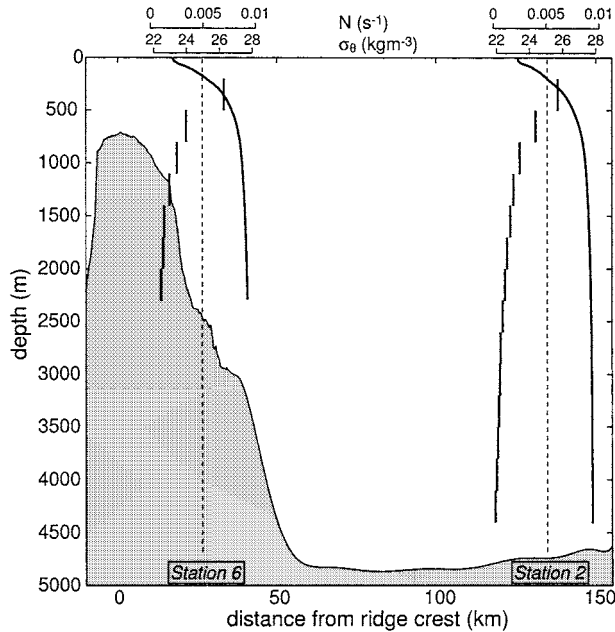


FIG. 2. Average potential density (σ_θ) and bin-averaged buoyancy frequency (N) at each station. The depth bins shown for N are used throughout the paper. The topographic section is along the line shown in Fig. 1.

with pressure, temperature, and conductivity sensors combine in the calculation of the vertical extent, L_z , of an overturn. However, the noise in each variable recorded at 24 Hz is significantly reduced, at the expense of spatial resolution, by averaging to 2 Hz. In the calculation of L_z , instrument noise is well below the resolution limit imposed by (1).

In many studies that consider overturning in stratified fluids (e.g., Thorpe 1977; Dillon 1982), temperature is regarded as the dominant stratifying species and overturns are sought in recorded temperature profiles. Kenan and Lukas (1996) have shown that lateral intrusions, with salinity-compensated temperature inversions, are common in certain portions of the water column at the HOT sites. For such intrusions, a temperature inversion is aligned with a salinity inversion, together resulting in a stable density profile. Therefore, in order to avoid false detection of nonexistent density inversions, we only use density profiles in our overturn detection analysis.

As above for L_z , limitations are also imposed by the resolution of density. In order to resolve the density extrema within an overturn, the signal resolution $\delta\rho$ of the 2-Hz data must be considerably less than the amplitude of the measured signal. We detrended and analyzed several deep (almost unstratified) data segments and determined an average value of $\delta\sigma_\theta = 0.5 \times 10^{-3} \text{ kg m}^{-3}$. With the density gradient (i.e., $d\rho/dz = \rho_0 g^{-1} N^2$), smoothed over scales of order 10 m, the signal resolution ($\delta\rho$) imposes a lower limit on the vertical

spatial resolution. Using a safety margin, Galbraith and Kelley (1996) suggested that no overturns thinner than

$$L_{\sigma_\theta, \min} = 2 \frac{g}{N^2} \frac{\delta\sigma_\theta}{\rho_0} \quad (2)$$

can be accurately resolved. For our instrumentation, the vertical resolution ranges from $L_{\sigma_\theta} = 0.2 \text{ m}$ for $N = 0.007 \text{ s}^{-1}$ in the upper pycnocline (see Fig. 2) to $L_{\sigma_\theta} = 10 \text{ m}$ for $N = 0.001 \text{ s}^{-1}$ near the bottom. Therefore, the vertical resolution, specified by (1), limits the detection of overturns in the upper water column and the density signal resolution, specified by (2), limits the detection of overturns near the bottom. Adhering to these criteria eliminates any spurious overturns that might otherwise result from instrument noise or ship motion.

2) OVERTURN DETECTION

In Figs. 3a and 3b, 2-Hz data segments are shown along with fitted spline representations. The temperature and salinity profiles were combined with an equation of state to form a spline representation of the potential density profile, $\sigma_\theta(z)$ (Fig. 3c). For depths less than 3000 m, a reference pressure of 0 dbar was used in the calculation, while for depths greater than 3000 m, a reference pressure of 4000 dbar was used.

The spline function $\sigma_\theta(z)$ was pointwise differentiated and solutions to $d\sigma_\theta/dz = 0$ were used to detect density extrema. An analysis of $d^2\sigma_\theta/dz^2$ was used in the detection of density maxima and a tracking algorithm was invoked to find the vertical limits of each overturn. Figure 3c demonstrates how the σ_θ values at the upper and lower bounds of an overturn correspond, respectively, with the minimum and maximum σ_θ values within the overturn. This definition of the vertical extent, L_z , of an overturn corresponds with the standard also used by Dillon (1982), Ferron et al. (1998), and others. It has the characteristic that the integral of the Thorpe displacement d' (see section 3a) over the depth of the overturn is equal to zero.

In our analysis, all overturns that exist within larger overturns are ignored as they are assumed to be perturbations within the encompassing structure. In addition, any overturns that overlap in the vertical are joined together.

3. Results

a. Thorpe scale

A transfer of energy from barotropic tidal motions to internal baroclinic tides through interaction with topography at the Hawaiian ridge has been previously inferred by the divergence of low-mode internal tides away from the ridge (Ray and Mitchum 1996, 1997). Further down this energy pathway, we anticipate that tidally generated internal waves lead to regions of enhanced shear, instability, and turbulent overturning. We are concerned with

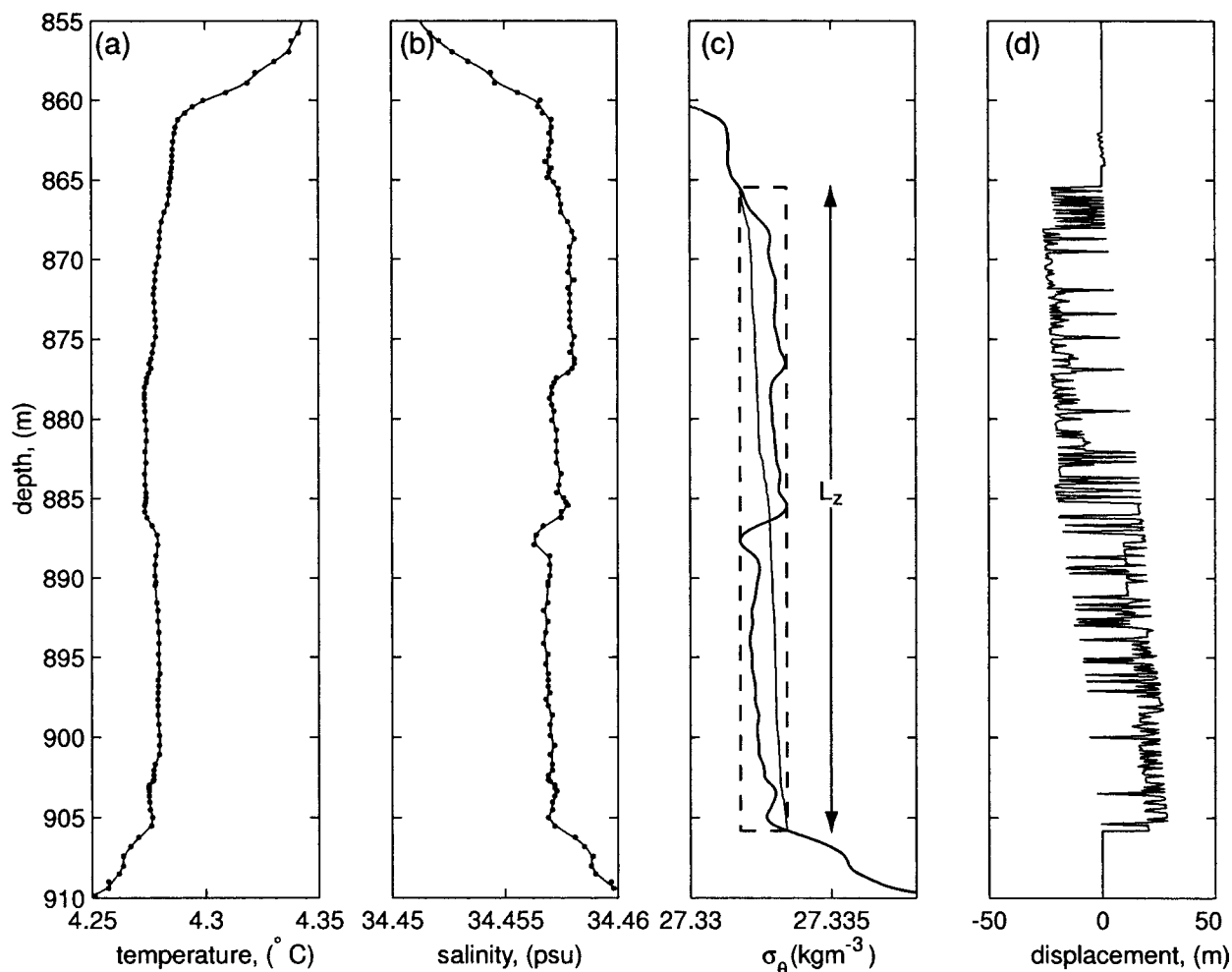


FIG. 3. A large overturn as observed in the CTD data from station 6. (a) Temperature profile from 2-Hz data (dots) and spline fit (thin line), (b) salinity profile from 2-Hz data (dots) and spline fit (thin line), (c) potential density profile (thick line) and Thorpe reordered profile (thin line), and (d) Thorpe displacement profile.

overturns having dimensions ($L_z \geq 2$ m) that can be considered as finescale or larger. As we show in section 3e, smaller structures do not contribute significantly to the volume averaged turbulent dissipation rate. By analyzing meter-scale phenomena to infer dissipation-scale processes we assume that the dissipation rate is dependent on the structure and energetics of the encapsulating overturn. Given the resolution limits of our measurements, we therefore seek to accurately quantify finescale processes and then relate the results to small-scale parameters such as the dissipation of turbulent kinetic energy, ε , and the turbulent diapycnal diffusivity, K_ρ .

The Thorpe scale L_T characterizes the vertical size of turbulent overturns and is indirectly related to dissipation-range turbulence (Dillon 1982). For each overturn, L_T is computed by reordering the density profile into a monotonic gravitationally stable profile. Each sample ρ_n within the original profile is associated with a depth z_n

and in the reordered profile with a depth z'_n . The difference is called the Thorpe displacement, $d'_n = z'_n - z_n$, and the Thorpe scale is defined as the root-mean-square of this quantity,

$$L_T = (\overline{d'^2})^{1/2}, \quad (3)$$

where the overbar denotes an average.

All overturns were detected in the measured profiles from stations 2 and 6, and those that did not satisfy the resolution criteria (section 2c) were ignored. Thorpe scales were computed by resampling at 0.1-m intervals along the σ_θ spline profiles for each overturn and then reordering the resulting data points. By this method, we are essentially filling in points between the measured 2-Hz data points and therefore do not expect to resolve the high wavenumber end of the Thorpe displacement spectrum. Nevertheless, the reordering process leads to accurate values of the Thorpe scale since larger displacements will be represented accurately and, as shown

by Stansfield et al. (2001), these are most important in the calculation of L_T .

The reordered profile for the sample overturn described above is shown as a thin line in Fig. 3c and the Thorpe displacements are shown in Fig. 3d. The displacement profile exhibits the inverted z shape that is a common characteristic of turbulent overturns (Dillon 1982).

Overturn data were organized into 300-m depth bins distributed from 200 m down to 2300 m at station 6 and down to 4400 m at station 2. The bins are shown in proximity to the average density profiles at station 2 and station 6 in Fig. 2.

The volume integrated dissipation rate which is achieved through overturning depends on both the number and size of overturns. The number of overturns that occurs, on average, in each 300 m vertical bin is shown in Fig. 4a. At station 6 the average number of overturns per observation varies from about seven near the top of the thermocline down to about two at 1000-m depth. Below this the number of overturns increases with depth to about four near the bottom. At station 2 we observe a similar decrease in overturn occurrence with depth in the upper water column. The average drops from about five above the thermocline to less than one at 2000 m. The interior region between 1000 and 2500 m is characterized by a distinct lack of overturning. Below this is a region of frequent overturning centered at about 3500 m. Near the bottom is a region of relatively few, but large (see below), overturns.

The average Thorpe scale is shown in Fig. 4b where we observe a steady increase with depth at station 6. Interestingly, there is a region of relatively large average Thorpe scale at the same depth (800–1100 m) as the minimum number of overturns. At station 2 there is a similar increase in $\overline{L_T}$ with depth. Here there is also a region of relatively large $\overline{L_T}$, which coincides spatially with a low occurrence rate of overturns (1700–2600 m).

Large Thorpe scales indicate enhanced mixing. In general, we observe an increase in both $\overline{N_{OT}}$ and $\overline{L_T}$ with depth near the bottom at both stations. This could be due to scattering of internal wave energy from bottom topography and local intensification due to interaction of incident and reflected waves, as well as friction-generated boundary shear. Such “bottom-generated” mixing has been observed in locations of significant bottom relief (e.g., Polzin et al. 1997) but not over seemingly benign topography such as at station 2. Lukas et al. (2001) have provided another explanation for near-bottom mixing in this region. They inferred near-bottom large eddy diffusivities at station 2 associated with episodic cold bottom water flows over the sill (at 4450 m) separating the Kauai Deep from the Maui Deep. Local intensification at interior depths might be due to other phenomena, such as internal wave rays that originate at the ridge.

b. Estimates of ε and K_ρ based on Thorpe scales

The Thorpe scale is a turbulence production range variable while the dissipation of turbulent kinetic energy ε is associated with microscale fluctuations. In order to relate these two quantities, it is often hypothesized that the large-scale overturn structure encases a patch of stratified turbulence with universal spectral properties. The Thorpe scale is then related to a dissipation length scale, particularly the Ozmidov length, $L_o = (\varepsilon/N^3)^{1/2}$. Here, L_o is essentially a large-scale representation of dissipation-scale processes. We cite the work of Dillon (1982), Ferron et al. (1998), Itsweire (1984), and Stansfield et al. (2001) who concur that L_T and L_o are correlated over a large range in both N and ε . The universality of the correlation remains a question, however, since measured values of the ratio L_o/L_T vary between studies from 0.65 to 0.95. For the present paper we use Dillon’s (1982) value of $L_o/L_T = 0.8$, which was shown to hold in a variety of mixing environments. It follows that the dissipation rate for a single overturning event is

$$\varepsilon_i = 0.64L_{Ti}^2N_i^3, \quad (4)$$

where N_i is the buoyancy frequency obtained from the gradient of the reordered potential density profile within the vertical boundaries of the i th overturn. This value of N represents the stratification against which work must be done in order to mix the fluid. As Alford and Pinkel (2000) have shown, overturns occur preferentially in small regions of low stratification (high strain), and the local N is thus required for correct application of (4). Overprediction of ε will result if the N_i are estimated as averages over depth intervals larger than L_{zi} .

The average dissipation rate over a vertical region H is given by

$$\varepsilon = \frac{\sum_i L_{zi}\varepsilon_i}{H}. \quad (5)$$

We form the ensemble average $\overline{\varepsilon}$ for each 300-m-depth bin (see Fig. 2) by including overturns from all CTD casts. Profiles of $\overline{\varepsilon}$ are shown in Fig. 4c. At station 6 the average dissipation rate is $0.43 \times 10^{-8} \text{ W kg}^{-1}$ in the thermocline (200–500 m), below which it decreases with depth to a value of $0.54 \times 10^{-9} \text{ W kg}^{-1}$ at 1000 m. There is then a slight increase with depth toward the bottom. Within 500 m from the bottom dissipation is enhanced by almost an order of magnitude above mid-depth levels. There is a similar decrease with depth down to 1500 m at station 2. However, dissipation rates are at least an order of magnitude smaller than at station 6, over this interval. This suggests that the topographic enhancement of mixing close to the ridge is distributed throughout the water column. Below 2000 m at station 2, there is an enhancement of the turbulence over a region spanning three 300-m-depth bins, focused most strongly at about 2500 m. This may be the signature of

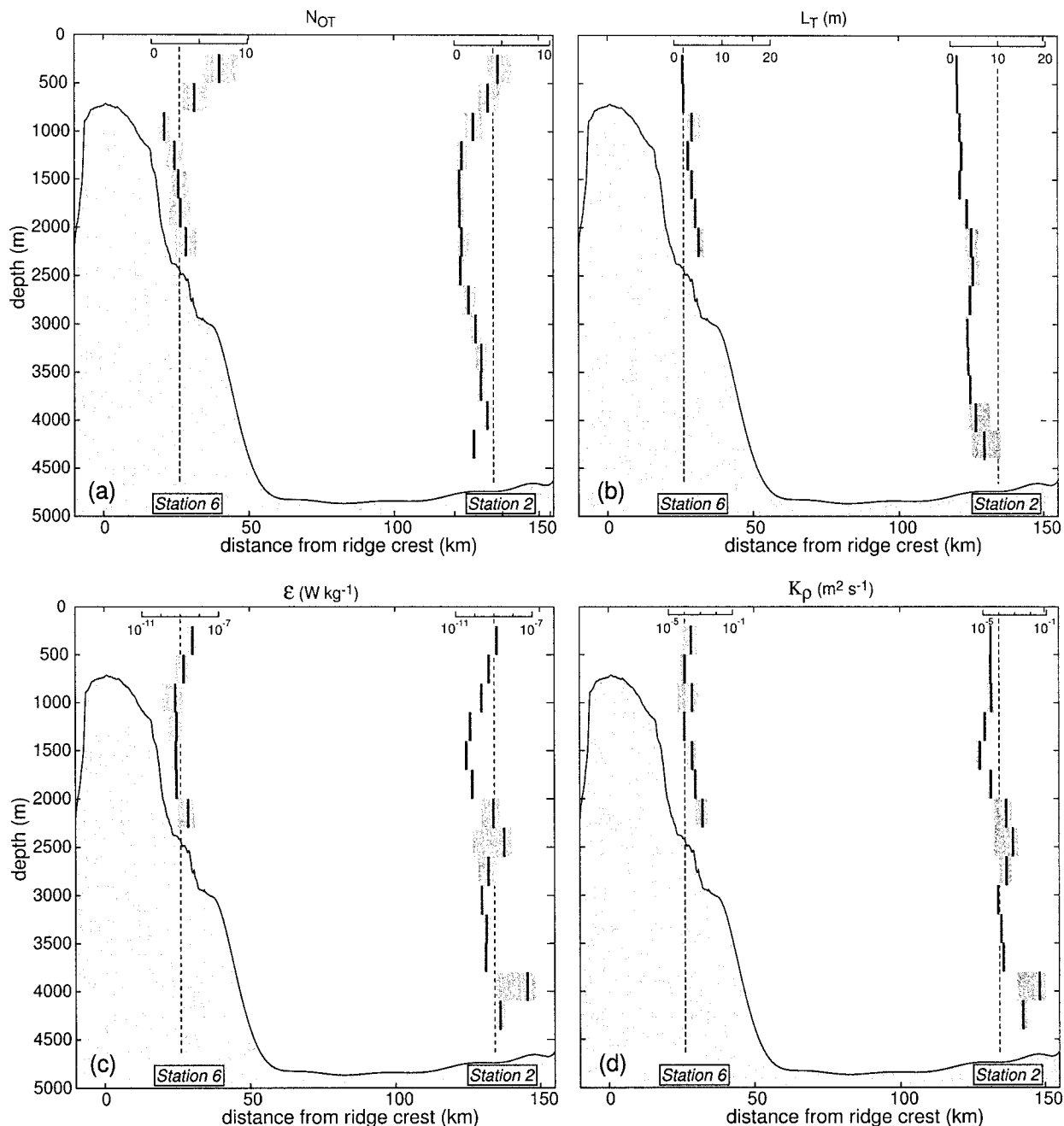


FIG. 4. Bin-averaged profiles for (a) the number of overturns per 300-m bin (N_{OT}), (b) Thorpe scale (L_T), (c) dissipation rate of turbulent kinetic energy (ϵ), and (d) turbulent diffusivity (K_ρ). The data profiles were measured along the dashed lines, which represent the locations of CTD profiles. The shaded regions span the 3d and 97th percentile for each bin, as determined from a bootstrapping technique using 1000 randomly sampled model datasets for each bin. If the data are assumed to be lognormally distributed, then the shaded areas approximate the 95% confidence interval (Toole et al. 1994).

mixing produced by an internal wave ray (see below). Dissipation rates reach high levels near the bottom at station 2 suggesting the presence of an active turbulent boundary layer. This is possibly related to episodic overflows from the nearby Maui Deep as found by Lukas et al. (2001). Boundary layer turbulence at station 2 appears to be more energetic than at station 6. However,

uncertainty is high in the near-bottom bins due to the difficulty of resolving $O(2\text{ m})$ overturns in very low stratification (see section 2c). Since only larger overturns are detected in the bottom bins, the average dissipation rate may be biased high. There is, nevertheless, a strong near-bottom signal. It is not clear if the source of this boundary layer turbulence is bottom shear from

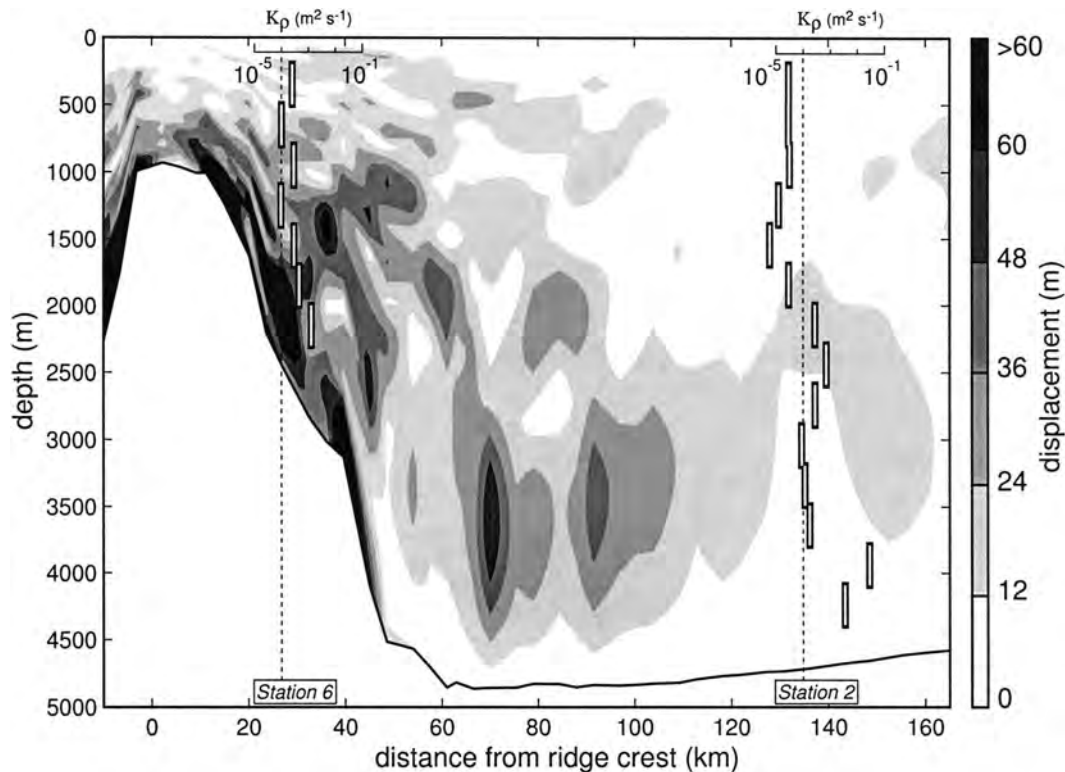


FIG. 5. Vertical isopycnal displacement (grayscale) from the numerical model of Merrifield et al. (2001) with profiles of K_ρ from the present study. The displacement values were extracted from the three-dimensional model results along the vertical section shown in Fig. 1.

barotropic motions, vertically propagating and interacting internal waves, or episodic deep overflows. Certainly, the enhanced mixing at middepth (2500 m) must be due to some internal wavelike phenomenon, such as an internal tidal ray.

We now consider the turbulent diapycnal diffusivity, K_ρ , which is closely related to the rate of mixing (or mass flux). Indeed, when multiplied by a vertical density gradient the resulting quantity represents a turbulent mass flux and is therefore a useful indicator of irreversible mixing. The most common model for K_ρ is due to Osborn (1980), who suggested

$$K_\rho = \frac{R_f}{1 - R_f} \frac{\varepsilon}{N^2}, \quad (6)$$

where R_f is the flux Richardson number, or the ratio of vertical advective flux to shear production. Osborn (1980) used the theoretical result of Ellison (1957) to suggest an upper bound of $R_f = 0.15$. Although the so-called mixing efficiency [$\Gamma = R_f/(1 - R_f)$] is not a constant and likely depends on the origin of the turbulence (e.g., Caldwell and Moum 1995), it is sufficient for our comparative analyses here to assume it is a constant. For our purposes, results for K_ρ were derived from ε using (5) and (6) with $\Gamma = 0.2$. The ensemble average \bar{K}_ρ was then formed using results from all overturns detected within a particular depth bin.

As shown in Fig. 4d, \bar{K}_ρ generally increases with depth at station 6 and has a depth-averaged value of $4 \times 10^{-4} \text{ m}^2 \text{ s}^{-1}$. At middepth the diffusivity is $1 \times 10^{-4} \text{ m}^2 \text{ s}^{-1}$ with some evidence for local intensification at about 1000 m. These values are roughly comparable, and slightly larger, than those found by Toole et al. (1997) above the flanks of Fieberling Guyot in the North Pacific.

At station 2 diffusivity is near typically observed low open ocean subthermocline background levels ($10^{-5} \text{ m}^2 \text{ s}^{-1}$) down to about 2000 m. There is evidence of a patch of enhanced mixing below this which, as mentioned above, could be due to an internal wave ray that emanates from the ridge 135 km away. To strengthen this proposition, we refer to Fig. 5 which shows the results for \bar{K}_ρ overlaid on an image of vertical displacement amplitude. The displacement data were extracted from the three-dimensional numerical model of Merrifield et al. (2001) along a section that passes through both stations 6 and 2. The enhanced mixing evidenced by large \bar{K}_ρ at station 2 around 2500 m is aligned with a band of heightened vertical displacement predicted by the model. It therefore appears that localized middepth mixing can be enhanced along tidal rays even at distances over 100 km from the generating topography. In this case, the enhanced mixing occurs at depths greater than 2000 m and below a region characterized by background

turbulence levels. In contrast, Toole et al. (1997) observed background levels of K_ρ throughout the water column at a distance of 15 km from Fieberling Guyot. This comparison implies that a ridge is probably much more effective at generating baroclinic waves than is an isolated seamount, a proposition demonstrated numerically by Holloway and Merrifield (1999). Although less clear, some correspondence between \bar{K}_ρ and displacement (η) is also seen at station 6 in Fig. 5.

At station 2, \bar{K}_ρ gradually increases toward the bottom. The values in the deepest two bins are of the same order of magnitude as those observed by Ferron et al. (1998) over sills and rough topography in the Romanche Fracture Zone. Since the bottom is relatively smooth at station 2, we suspect that the turbulence found here is due to the interaction of vertically propagating waves and/or to lee waves and shear associated with bottom water flowing over a sill from the Maui Deep into the broad Kauai Deep, as suggested by Lukas et al. (2001).

c. Vertical strain

Internal waves cause isopycnal displacements that contribute to the nonuniformity of observed vertical profiles of potential density. Vertical strain represents the gradient of isopycnal displacement and is often used as a measure of internal wave activity (e.g., Desaubies and Gregg 1981). By employing a parameterization of dissipation based on internal wave-induced strain, we now investigate another method of estimating small-scale mixing activity from large-scale density structure. The results will be compared below with L_T -based predictions. We begin by describing observed strain spectra at both stations, relative to canonical background levels.

Density profiles were separated into 300-m-depth segments (corresponding to the depth bins in Fig. 2), within which the buoyancy frequency is roughly constant, thereby avoiding spurious small-wavenumber contributions to strain. Individual profiles of σ_θ were detrended and normalized by the mean vertical potential density gradient $\overline{d\sigma_\theta/dz}$, calculated over each depth segment using a 10-m finite difference, resulting in profiles of vertical displacement, $\eta(z)$. Before computing the spectra, the overturn regions were resorted resulting in gravitationally stable profiles. The strain spectra ϕ_λ were computed from displacement spectra as

$$\phi_\lambda = (2\pi k)^2 \phi_\eta(k), \quad (7)$$

where k is the vertical wavenumber. Spectra from each station were averaged over all profiles and the results are shown in Fig. 6 for depth bins down to 3800 m. Near-bottom bin spectra from both stations have been omitted because of large uncertainty in strain estimates associated with small vertical density gradients.

For comparison, we also plot background levels as predicted by GM76 [from the model by Garrett and Munk (1975) as modified by Cairns and Williams

(1976)]. For GM76, the spectrum of vertical displacement is given by

$$\phi_\eta(\beta) = \frac{Eb^3 \left(\frac{N_o}{N}\right)^2}{2\pi j_*} \frac{1}{(1 + \beta/\beta_*)^2}, \quad \left[\frac{\text{m}^2}{\text{rad m}^{-1}} \right], \quad (8)$$

where β is the vertical wavenumber in radians per meter, $E = 6.3 \times 10^{-5}$ is the dimensionless energy level, $b = 1300$ m is the scale depth of the thermocline, and $N_o = 0.00524$ rad s $^{-1}$ is the reference buoyancy frequency corresponding to 3 cycles per hour. We use the reference wavenumber $\beta_* = 0.0073(N/N_o)$ rad m $^{-1}$ and the reference mode number $j_* = 3$ (see Gregg and Kunze 1991). With these definitions, the GM76 vertical strain spectra are

$$\phi_\lambda = \beta^2 \phi_\eta(\beta), \quad \left[\frac{1}{\text{rad m}^{-1}} \right]. \quad (9)$$

For comparison with observed spectra, we convert (9) to cyclic wavenumbers ($k = \beta/2\pi$).

Referring to Fig. 6 we note that spectra are resolved over nearly two decades in wavenumber space, which corresponds to wavelengths ranging from about 100 m down to about 3 m. The sharp increase in negative slope at $k = 0.3$ cpm is due to resolution limitations.

The spectra at all depths and at both stations have levels above GM76. Over some depth intervals the elevation at station 2 is slight, which indicates that in terms of strain, station 2 is (on average) in a near open-ocean state. The topographical effect of the ridge is clearly apparent in the strain spectra for station 6. It elevates the strain levels above those at station 2 for all wavenumbers and at all depths. The bottom frames in Fig. 6 show strain spectra in the deeper portion of the water column at station 2. In general, strain spectra correspond to GM76 background levels. However, from 2000 to 2900 m for $k < 0.5$ cpm, the spectral energy levels become slightly elevated, not inconsistent with the previous identification of enhanced turbulence at these depths (Fig. 4).

d. Estimates of ε based on strain

Several models now exist for estimating the dissipation rate of turbulent kinetic energy, due to wave-wave interaction, in the open ocean (see Polzin et al. 1995; Wijesekera et al. 1993). These generally rely on the existence of a canonical open-ocean internal wave field as described by Garrett and Munk (1975). However, Wijesekera et al. (1993) have shown that such models can also provide reasonable predictions of ε in particularly energetic regions (non-GM wave fields) if the vertical wavenumber bandwidth parameter, β_* , is explicitly retained. Adopting their formulation for strain-based models, we assume

$$\varepsilon_\lambda = 7 \times 10^{-10} \frac{\langle N^2 \rangle}{N_o^2} \frac{\langle \lambda_{10}^2 \rangle^2}{(\lambda_{10,GM}^2)^2}, \quad [\text{m}^2 \text{ s}^{-3}], \quad (10)$$

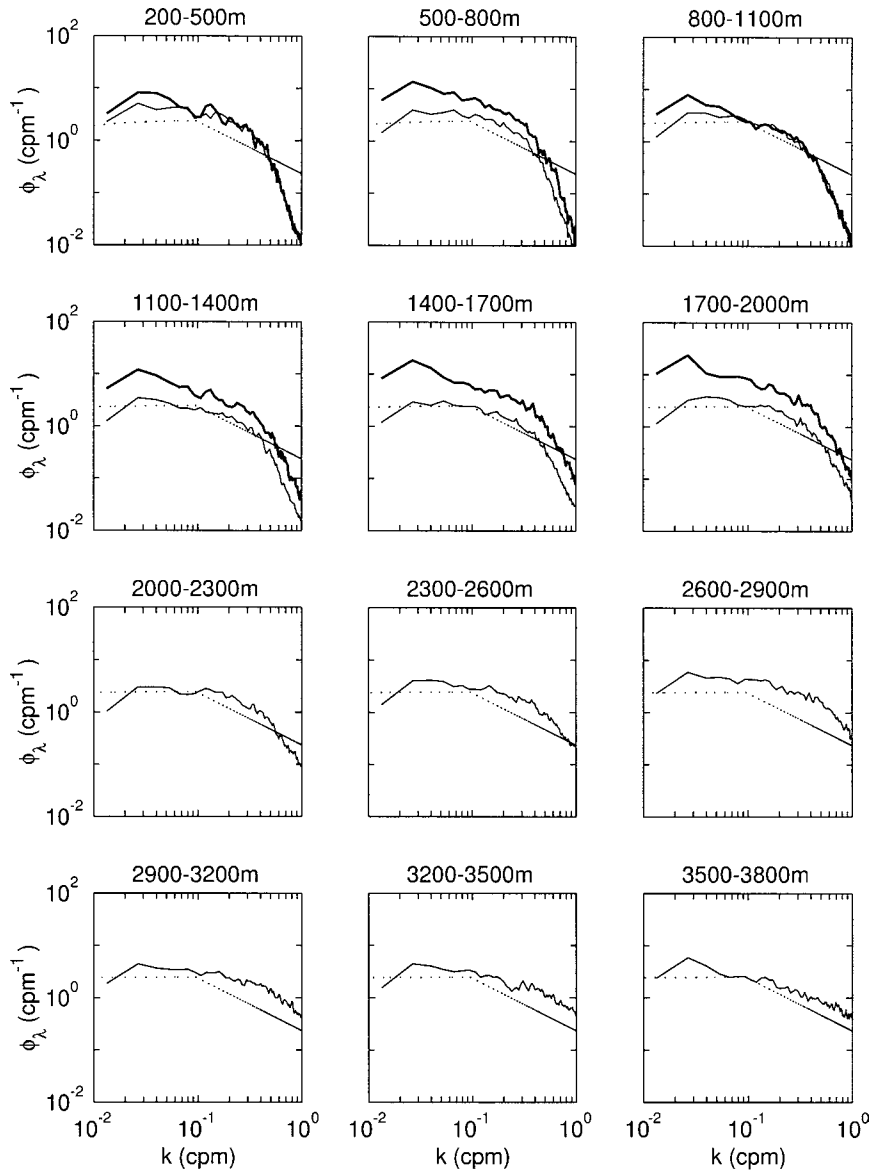


FIG. 6. Measured spectra of vertical strain at both stations along with GM76 model spectra (dotted line). The panels represent depth bins down to 3800 m. Spectra from station 6 (thick line) are generally elevated above spectra from station 2 (thin line) and GM76.

where λ_{10} is the strain evaluated by integrating the spectra of section 3c from small wavenumbers to $k_u = 0.1$ cpm, corresponding to a length scale of 10 m; $\lambda_{10,GM}^2$ is the variance of 10-m strain in a GM76 wave field with canonical energy density. This quantity was calculated by Gregg and Kunze (1991) as

$$\lambda_{10,GM}^2 = \frac{\pi E b j_* \beta_u}{2}, \quad (11)$$

where $\beta_u = 2\pi k_u$ is the radian wavenumber corresponding to a 10-m length scale.

In Fig. 7 we present the ratio of Thorpe scale-based dissipation rate estimates to strain-based estimates.

Near-bottom data are again omitted due to large uncertainty in strain spectra estimates. Both methods give similar predictions for $\bar{\varepsilon}$ at station 6. Values are within a factor of 2 at all depths, in fact $0.5 < \varepsilon_{L_T}/\varepsilon_\lambda < 1.5$. At station 2, the strain method estimates slightly higher values than the L_T method down to a depth of 1700 m. Nevertheless, both estimates are within a factor of 2 over this depth range. Below this, the strain method appears to underestimate ε (assuming L_T gives roughly accurate predictions) as the stratification decreases with depth. Therefore, it appears that the strain-based model is a reasonable predictor of ε for $N > 0.001 \text{ s}^{-1}$. Where the stratification is weak, strain is either underresolved

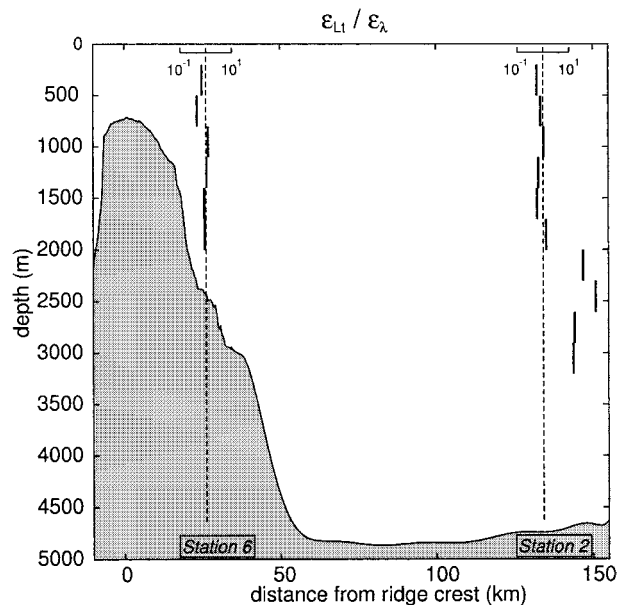


FIG. 7. Profiles of the ratio of dissipation rates derived from Thorpe scales to those derived from strain estimates.

or simply a poor predictor of turbulence production. We regard the Thorpe scale as a more robust indicator as it explicitly accounts for the potential energy available for turbulence production which in turn should be related to mixing. However, it is sensitive to instrument noise, particularly in weak stratification.

Since the density profiles are reordered into gravitationally stable profiles prior to computing strain spectra, the potential energy available for turbulence production is essentially removed. In contrast, it is this energy that is directly reflected in the Thorpe scale analysis. This difference may account for some of the discrepancy between strain and L_T -based estimates of $\bar{\varepsilon}$. High strain may be a required precursor to overturning (Alford and Pinkel 2000) but does not appear to be a robust indicator of mixing in general. Nevertheless, we conclude that strain can provide reasonable estimates in unenergetic regions where N is greater than about 0.001 s^{-1} .

e. Large mixing events

Alford and Pinkel (2000) reported the size distribution of overturns in the thermocline (0–400 m) of an energetic coastal region. They evaluated ε using the Thorpe scale method and then computed the conditional sum

$$C_{L_T}(x) \equiv \sum_{i|L_{T_i} < x} \varepsilon_{T_i} L_{z_i} / \bar{\varepsilon}_T, \quad (12)$$

which gives the fractional contribution to overall dissipation from events with Thorpe scales less than x . They also applied a minimum overturn size restriction of 2 m. From their analysis they concluded that the small

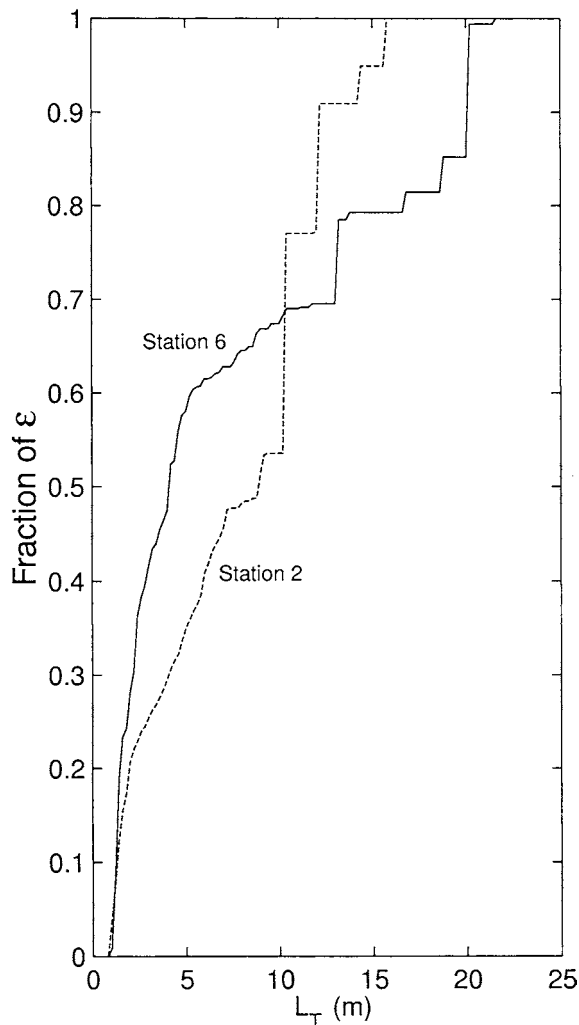


FIG. 8. Contribution to the overall dissipation from different sizes of overturns. Large events contribute significantly to the overall dissipation rate found at both stations.

overturns that are not accounted for only contribute about 10% to the total ε . About 80% of the dissipation was achieved through overturns with $L_z < 8$ m. Larger overturns (>10 m) contributed less than 10%.

The distribution studied by Alford and Pinkel (2000) appears to reflect an energetic mixing regime in a strongly stratified environment in the upper ocean (100–400 m). In comparison, the distribution at station 6 (for the depth range 200–2300 m; see Fig. 8) reflects a more moderate mixing regime. Here we find that less than 65% of the dissipation is achieved by overturns with Thorpe scale less than 8 m. The distribution amongst the size classes is continuous only for $L_T < 13$ m which accounts for about 70% of the total dissipation. The remaining 30% is due to a small number of large isolated mixing events, which appear as steps in the graph of Fig. 8. Each overturn in this size class contributes a significant proportion to the overall dissipation. The

large overturning events have Thorpe scales of $L_T = 13$ to 22 m and vertical patch sizes of up to $L_z = 40$ m. The local dissipation rate associated with the largest observed overturn at station 6 was $\varepsilon = 1 \times 10^{-6}$ W kg^{-1} with $K_p = 2 \times 10^{-3}$ $\text{m}^2 \text{s}^{-1}$. At station 2 (for the depth range 200–3800 m) there are signs of a weaker mixing regime. Here, less than 50% of the dissipation is due to overturns with $L_T < 8$ m. Large events account for the remaining mixing. Although they account for a larger proportion of the overall dissipation, the isolated mixing events at station 2 are generally smaller and weaker than at station 6. For example, note the station 2 event shown in Fig. 8 with $L_T = 10$ m. This single event accounts for nearly 25% of the total dissipation at station 2. (Note that 617 and 385 overturns contribute to the distributions of ε at stations 2 and 6, respectively.)

4. Some evidence for tidal modulation of mixing intensity

We have focused above on spatiotemporal averages of mixing characteristics in the vicinity of the Hawaiian ridge. It is also of interest to determine if there is a detectable temporal variability associated with the generation of internal tides at the ridge. If such a signal exists in our data, then it is most likely to be found at station 6. After several attempts to view a correlation between predicted barotropic tidal currents (from TPX0.3 and TPX0.5; see Egbert 1997) and temporal variations in estimated ε , we determined that the two processes are too far removed in time and space to form a statistically significant correlation. We thus turned our attention to internal motions with the hope that vertical displacements are more closely coupled with mixing.

a. Inverted echo sounder data

An inverted echo sounder (IES) was moored on the ocean floor at station 6 during 1994–95, corresponding with the time period when our CTD observations were made. The instrument measured the round-trip acoustic travel time (τ) from the seafloor to the surface and back. A continuous record of τ was recorded and the data were corrected for barotropic tidal sea level fluctuations. As explained by Watts and Rossby (1977), it is assumed that τ is highly correlated with dynamic height and that it is only sensitive to low vertical mode variability. Therefore, at tidal frequencies variations in the τ signal reflect isopycnal displacements associated with low-mode internal waves.

Rather than apply an ad hoc calibration to convert our data to displacements, we simply plot the τ time series (in units of seconds) as a means of viewing the internal tide activity. As shown in Fig. 9, this time series has signatures of regular tidal variability, such as spring–neap cycles, as anticipated.

b. K_p as a function of τ (displacement)

The times at which CTD casts were performed are shown on the τ time series in Fig. 9 as vertical lines. Values of ε derived from the CTD data by the Thorpe scale method of section 3b are represented as circles above and below the τ time series. For each cast, the upper circles represent the average ε for the depth segment 200–1100 m and the lower circles represent ε for the depth segment 1100–2000 m (where the near-bottom depth bin, 2000–2300 m, has been excluded to avoid the inclusion of spurious overturns due to low stratification and bottom boundary layer effects). A correspondence between τ and ε is not clearly evident as the mixing, particularly in the upper depth segment, is strongly influenced by sporadic large mixing events. The large events do tend to follow peaks in the τ time series and they generally occur at, or shortly after, the peak in the spring tide.

In an effort to relate tidal activity to mixing statistics derived from each CTD cast, we developed a simple method for associating particular values of τ with ε observations. For each cast we determined the maximum value of τ that occurred within a 12-h time window centered at 10 h prior to the cast. This τ value is associated with the value of ε determined from the CTD cast. The reasoning here is that a peak in the displacement corresponds to relatively large shear, and small strain, conditions favorable to the growth of instabilities and possible overturning. Of course, τ is a measure of only the largest vertical-scale variability and there is no guarantee that the small vertical-scale tidal fluctuations, which may generate the turbulence, have amplitude modulations that are always correlated with the amplitude modulations of the large vertical-scale internal tides. The offset time window was positioned to allow for a shear instability growth-and-collapse timescale of order 8 h (see Alford and Pinkel 2000). It is thus assumed that overturns we observe during a cast are associated with a peak in the vertical displacement that occurred between 16 and 4 h prior to the cast. This concept is also supported by the results of Ledwell et al. (2000) who observed a 1–2-day phase lag between the dissipation rate and the barotropic tidal current speed over the rough topography in the eastern Brazil Basin.

Figure 10 shows the resulting dependence of ε on τ for both depth segments, 200–1100 and 1100–2000 m. There appears to be little, if any, correlation between mixing and τ within the lower depth region. In contrast, over the depth range 200–1100 m there is some evidence that large τ (i.e., large tidally induced isopycnal displacement) has an enhancing effect on the mixing. As we have seen in section 3e, the value of ε can be influenced substantially by rather infrequent large events and the scatter in Fig. 10 tends to reflect this. Assuming that variability in τ is dominated by tidal variability, which it appears to be from Fig. 9, then the large mixing events may be triggered during periods of strong bar-

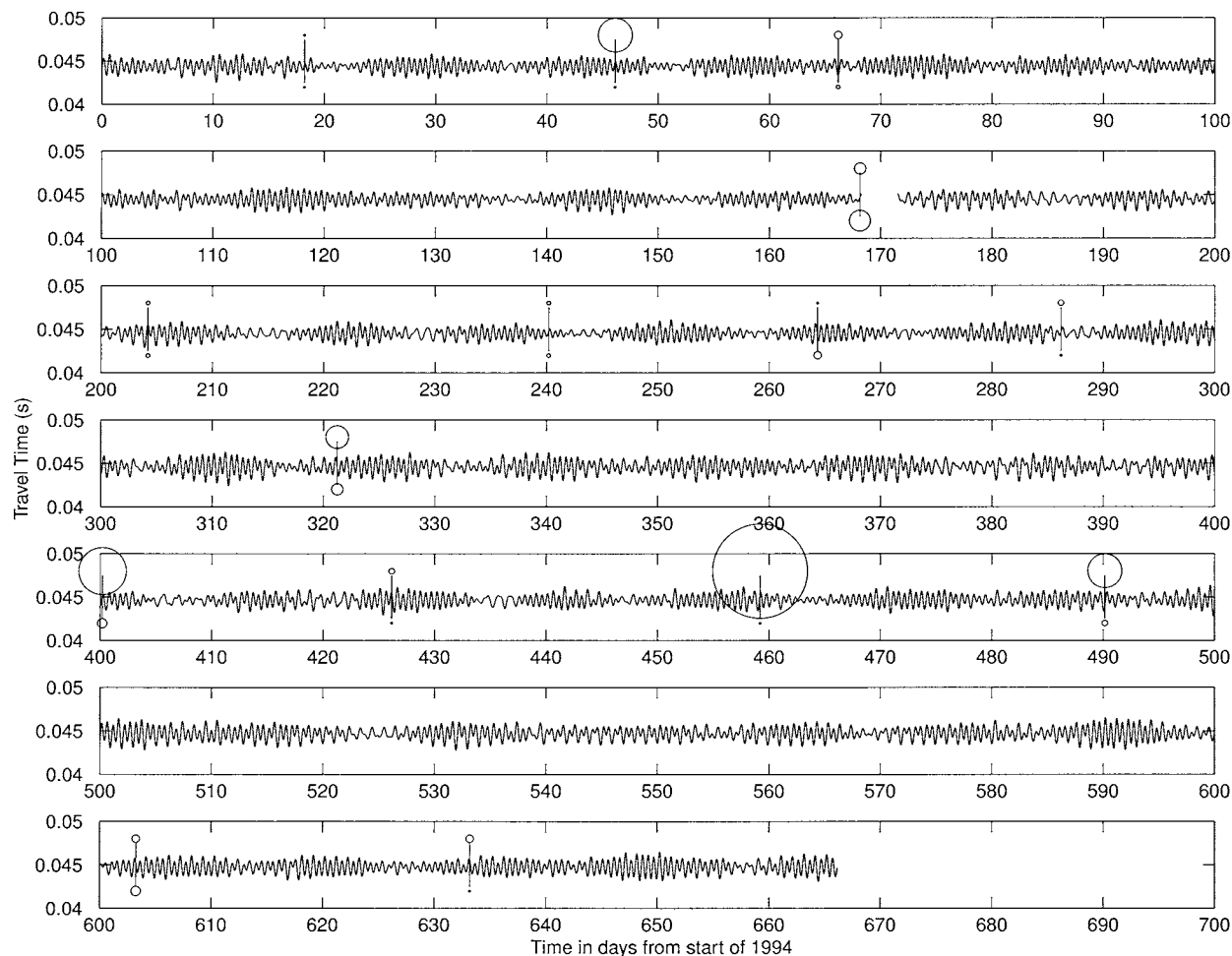


FIG. 9. Time series of IES acoustic travel time (τ) at station 6. This signal reflects the amplitude of low mode isopycnal displacements. CTD casts are shown as vertical bars and depth averaged dissipation rate (ϵ), at each cast, is shown above the τ line for the upper water column (200–1100 m) and below the τ line for the lower water column (1100–2000 m). The size of the circle indicates the relative magnitude of ϵ .

otrophic tidal fluctuations. The largest fluctuations are found during spring tide so a fortnightly modulation of the mixing intensity may occur here, although our data lack the temporal resolution to examine this. A fortnightly modulation of mixing has been observed previously by Ledwell et al. (2000) in the Brazil Basin. The variability of mixing on shorter (diurnal) timescales has been investigated by Lien and Gregg (2001) at the continental shelf edge near Monterey Bay, California, with results suggesting a tidal modulation of ϵ values, though the scatter in ϵ is large like Fig. 10 here.

5. Conclusions

An analysis of turbulent overturns has revealed heightened levels of mixing at all depths over the slope of the Hawaiian ridge and in an isolated middepth segment (and maybe near the bottom) at a deep-water station 135 km north of the ridge. Results, derived from 15 independent CTD casts performed at station 6, in-

dicate that the average number of observed overturns decreases with depth from the surface to a minimum at middepth, and then increases again toward the bottom. A similar distribution was also found at station 2 in the deep ocean. Such patterns are probably associated with the unique features of this region, such as tidal rays emanating from the ridge and deep water flows over interbasin sills. The same vertical distribution is not mimicked by the Thorpe scale, which was observed to increase steadily with depth over the entire water column except for a localized middepth increase that is apparent at both stations.

As shown in Fig. 4c, profiles of the rate of dissipation of turbulent kinetic energy exhibit features of both N_{OR} and L_T distributions. Over the slope of the ridge the average dissipation rate ranged from $\epsilon = 4 \times 10^{-9} \text{ W kg}^{-1}$ in the thermocline and near the bottom to about $\epsilon = 0.5 \times 10^{-9} \text{ W kg}^{-1}$ in the interior. These levels of heightened dissipation rate are comparable to those found by Toole et al. (1997) over the flanks of Fieberling

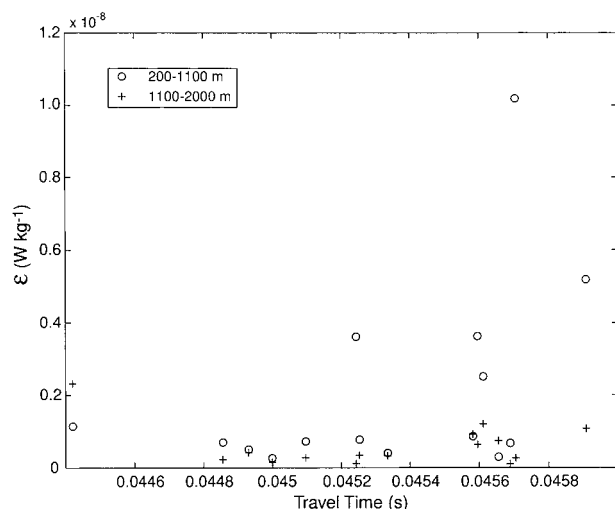


FIG. 10. The rate of dissipation of kinetic energy (ϵ) as a function of the IES acoustic travel time (isopycnal displacement) at station 6. Open circles represent results for the upper water column (200–1100 m) and crosses for the lower water column (1100–2000 m).

Guyot in the North Pacific. Perhaps more interesting are the results from the far field. Toole et al. (1997) found near-background levels of dissipation at a distance of 15 km from the seamount. Our results also indicate near background levels at station 2, 135 km from the crest of the Hawaiian ridge, only down to a depth of 2000 m. Below this we observe a zone of enhanced mixing. A comparison with the numerical results of Merrifield et al. (2001) suggests that this enhancement is due to the presence of an internal tidal ray. Within this zone we estimate that $\epsilon \sim O(10^{-9}) \text{ W kg}^{-1}$ and $K_p \sim O(10^{-4}) \text{ m}^2 \text{ s}^{-1}$ or slightly larger. The mixing inferred at both stations confirms that the Hawaiian ridge scatters enough energy into baroclinic modes to cause enhanced mixing both near the topography and, to a lesser extent, at 135 km away. The estimates of Toole et al. (1997) indicate that these levels of enhanced mixing near topography have relevance to the large-scale circulation of the abyssal ocean but it remains to be determined if such localized mixing balances vertical advection at oceanic scales.

Application of a strain-based wave–wave interaction model produced dissipation estimates that were similar to Thorpe scale–derived estimates except in regions of weak stratification. The exact reason for this discrepancy is unclear. While the Thorpe scale method will be affected by the limited resolution of the CTD measurements, through the possible misinterpretation of noise variability as overturns, we have been very conservative in our analyses in order to minimize this possibility. Even in the bottom 1000 m at station 2, where the stratification is weakest, our Thorpe-based estimates of mixing are in good agreement with independent estimates by Lukas et al. (2001). The order of magnitude discrepancies below 2000 m between the two methods of

estimating ϵ shown in Fig. 7 at station 2 are not believably due to overestimates of the Thorpe scale. Thus, we suspect the strain-based method is greatly underestimating ϵ in regions of weak stratification.

The mixing regime near Hawaii is influenced as much by infrequent large overturning events as it is by frequent small events. It appears that the large overturning events, and high dissipation rates, are triggered by large tidal amplitudes associated with the spring tide. It is still necessary to determine if the mixing near Hawaii is modulated on shorter timescales by the semidiurnal tide. A clearer picture of the spatial and temporal distribution of mixing, and the structure and impact of internal tide rays, could be revealed by more comprehensive observational studies. Such studies are underway as part of the Hawaii Ocean Mixing Experiment (Pinkel et al. 2000) and forthcoming results will surely add to what has been presented here.

Acknowledgments. We thank Shaun Johnston and Mark Merrifield for providing the displacement data shown in Fig. 5, and Sharon DeCarlo and Fernando Santiago-Mandujano for furnishing the 2-Hz CTD and IES data. Thanks also to Gary Egbert for providing the TPX0.5 tidal analyses and Brian Dushaw for a user-friendly GUI to manipulate the TPX0.5 output. Eric Kunze provided detailed comments on an earlier version of the manuscript, which greatly improved the exposition. We also thank Walter Munk and an anonymous reviewer for helpful comments. This work was supported by the U.S. National Science Foundation under Grant OCE 98-19517 as part of the Historical Data Analysis component of the Hawaii Ocean Mixing Experiment, and by NSF Grant OCE-9811921 for the Hawaii Ocean Time Series.

REFERENCES

- Alford, M. H., and R. Pinkel, 2000: Observations of overturning in the thermocline: The context of ocean mixing. *J. Phys. Oceanogr.*, **30**, 805–832.
- Armi, L., 1978: Some evidence for boundary mixing in the deep ocean. *J. Geophys. Res.*, **83**, 1971–1979.
- Bell, T. H., 1975: Lee waves in stratified flows with simple harmonic time dependence. *J. Fluid Mech.*, **67**, 705–722.
- Cairns, J. L., and G. O. Williams, 1976: Internal wave observations from a midwater float. *J. Geophys. Res.*, **81**, 1943–1950.
- Caldwell, D. R., and J. N. Moum, 1995: Turbulence and mixing in the ocean. *Rev. Geophys.*, **33** (Suppl.), 1385–1394.
- Desaubies, Y., and M. C. Gregg, 1981: Reversible and irreversible finestructure. *J. Phys. Oceanogr.*, **11**, 541–556.
- Dillon, T. M., 1982: Vertical overturns: A comparison of Thorpe and Ozmidov scales. *J. Geophys. Res.*, **87**, 9601–9613.
- Egbert, G. D., 1997: Tidal data inversion: Interpolation and inference. *Progress in Oceanography*, Vol. 40, Pergamon, 53–80.
- Ellison, T. H., 1957: Turbulent transport of heat and momentum from an infinite rough plane. *J. Fluid Mech.*, **2**, 456–466.
- Eriksen, C. C., 1985: Implications of ocean bottom reflection for internal wave spectra and mixing. *J. Phys. Oceanogr.*, **15**, 1145–1156.
- Ferron, B., H. Mercier, K. Speer, A. Gargett, and K. Polzin, 1998:

- Mixing in the Romanche Fracture Zone. *J. Phys. Oceanogr.*, **28**, 1929–1945.
- Galbraith, P. S., and D. E. Kelley, 1996: Identifying overturns in CTD profiles. *J. Atmos. Oceanic Technol.*, **13**, 688–702.
- Garrett, C., 1991: Marginal mixing theories. *Atmos.–Ocean*, **29**, 313–339.
- , and W. H. Munk, 1975: Space–time scales of internal waves: A progress report. *J. Geophys. Res.*, **80**, 291–297.
- Gregg, M. C., 1987: Diapycnal mixing in the thermocline: A review. *J. Geophys. Res.*, **92**, 5249–5286.
- , and E. Kunze, 1991: Shear and strain in Santa Monica Basin. *J. Geophys. Res.*, **96**, 16 709–16 719.
- Holloway, P. E., and M. A. Merrifield, 1999: Internal tide generation by seamounts, ridges and islands. *J. Geophys. Res.*, **104**, 25 937–25 951.
- Itsweire, E. C., 1984: Measurements of vertical overturns in a stably stratified turbulent flow. *Phys. Fluids*, **27**, 764–766.
- Karl, D. M., and R. Lukas, 1996: The Hawaii Ocean Time-Series (HOT) program—Background, rationale and field implementation. *Deep-Sea Res.*, **43B**, 129–156.
- Kennan, S. C., and R. Lukas, 1996: Saline intrusions in the intermediate waters north of Oahu, Hawaii. *Deep-Sea Res.*, **43B**, 215–241.
- Ledwell, J. R., E. T. Montgomery, K. L. Polzin, L. C. St. Laurent, R. W. Schmitt, and J. M. Toole, 2000: Evidence for enhanced mixing over rough topography in the abyssal ocean. *Nature*, **403**, 179–182.
- Lien, R. C., and M. C. Gregg, 2001: Observations of turbulence in a tidal beam and across a coastal ridge. *J. Geophys. Res.*, **106**, 4575–4591.
- Lukas, R., and F. Santiago-Mandujano, 1996: Interannual variability of Pacific deep and bottom waters observed in the Hawaii Ocean time series. *Deep-Sea Res.*, **43B**, 243–255.
- , —, F. Bingham, and A. Mantyla, 2001: Cold bottom water events observed in the Hawaii Ocean time series: Implications for vertical mixing. *Deep-Sea Res.*, **48**, 995–1021.
- Merrifield, M. A., P. E. Holloway, and T. S. Johnston, 2001: The generation of internal tides at the Hawaiian Ridge. *Geophys. Res. Lett.*, **28**, 559–562.
- Munk, W. H., 1966: Abyssal recipes. *Deep-Sea Res.*, **13**, 207–230.
- , and C. Wunsch, 1998: Abyssal recipes II: Energetics of tidal and wind mixing. *Deep-Sea Res.*, **45**, 1978–2010.
- Osborn, T. R., 1980: Estimates of the local rate of vertical diffusion from dissipation measurements. *J. Phys. Oceanogr.*, **10**, 83–89.
- Phillips, O. M., 1977: *The Dynamics of the Upper Ocean*. 2d ed. Cambridge University Press, 336 pp.
- Pinkel, R., and Coauthors, 2000: Ocean mixing studies near the Hawaiian ridge. *Eos. Trans. Amer. Geophys. Union*, **81**, 545–553.
- Polzin, K. L., J. M. Toole, and R. W. Schmitt, 1995: Finescale parameterizations of turbulent mixing. *J. Phys. Oceanogr.*, **25**, 306–328.
- , —, J. R. Ledwell, and R. W. Schmitt, 1997: Spatial variability of turbulent mixing in the abyssal ocean. *Science*, **276**, 93–96.
- Ray, R. D., and G. T. Mitchum, 1996: Surface manifestations of internal tides generated near Hawaii. *Geophys. Res. Lett.*, **23**, 2101–2104.
- , and —, 1997: Surface manifestation of internal tides in the deep ocean: Observations from altimetry and island gauges. *Progress in Oceanography*, Vol. 40, Pergamon, 135–162.
- Santiago-Mandujano, F., L. Tupas, C. Nosse, D. Hebel, L. Fujieki, R. Lukas, and D. Karl, 1999: Hawaii Ocean Time Series Data Report 10, 1998. SOEST Tech. Rep. 99-5, School of Ocean and Earth Science and Technology, University of Hawaii, Honolulu, HI, 246 pp.
- Stansfield, K., C. Garrett, and R. Dewey, 2001: The probability distribution of the Thorpe displacement within overturns in Juan de Fuca Strait. *J. Phys. Oceanogr.*, **31**, 3421–3434.
- Thorpe, S. A., 1973: Experiments on instability and turbulence in a stratified shear flow. *J. Fluid Mech.*, **32**, 693–704.
- , 1977: Turbulence and mixing in a Scottish loch. *Philos. Trans. Roy. Soc. London*, **286A**, 125–181.
- Toole, J. M., K. L. Polzin, and R. W. Schmitt, 1994: Estimates of diapycnal mixing in the abyssal ocean. *Science*, **264**, 1120–1123.
- , R. W. Schmitt, K. L. Polzin, and E. Kunze, 1997: Near-boundary mixing above the flanks of a midlatitude seamount. *J. Geophys. Res.*, **102**, 947–959.
- Watts, D. R., and H. T. Rossby, 1977: Measuring dynamic heights with inverted echo sounders: Results from MODE. *J. Phys. Oceanogr.*, **7**, 346–358.
- Wijesekera, H., L. Padman, T. Dillon, M. Levine, and C. Paulson, 1993: The application of internal-wave dissipation models to a region of strong mixing. *J. Phys. Oceanogr.*, **23**, 269–286.
- Winters, K. B., and E. A. D’Asaro, 1996: Diascalar flux and the rate of fluid mixing. *J. Fluid. Mech.*, **317**, 179–193.